Pergamon

Geochimica et Cosmochimica Acta, Vol. 67, No. 10, pp. 1787–1801, 2003

0016-7037/03 $30.00 + .00

doi:10.1016/S0016-7037(02)01305-4

Connections between surface complexation and geometric models of mineral dissolution investigated for rhodochrosite

OWEN W. DUCKWORTH and SCOT T. MARTIN*

Division of Engineering and Applied Sciences, Pierce Hall, 29 Oxford Street, Harvard University, Cambridge, MA 02138, USA

(*Received May* 3, 2002; *accepted in revised form October* 16, 2002)

Abstract—Mineral dissolution rates have been rationalized in the literature by surface complexation models (SCM) and morphological and geometric models (GM), and reconciliation of these conceptually different yet separately highly successful models is an important goal. In the current work, morphological alterations of the surface are observed in real time at the microscopic level by atomic force microscopy (AFM) while dissolution rates are simultaneously measured at the macroscopic level by utilizing the AFM fluid cell as a classic flow-through reactor. Rhodochrosite dissolution is studied from pH = 2 to 11 at 298 K, and quantitative agreement is found between the dissolution rates determined from microscopic and macroscopic observations. Application of a SCM model for the interpretation of the kinetic data indicates that the surface concentration of $>CO_3H$ regulates dissolution for pH < 7 while the surface concentration of $>MnOH_2^+$ regulates dissolution for pH > 7. A GM model explains well the microscopic observations, from which it is apparent that dissolution occurs at steps associated with anisotropic pit expansion. On the basis of the observations, we combine the SCM and GM models to propose a step-site surface complexation model (SSCM), in which the dissolution rates are quantitatively related to the surface chemical speciation of steps. The governing SSCM equation is as follows: $R = \chi_{1/2}(k_{co} + k_{ca})[>CO_3H] + \chi_{1/2}(k_{mo} + k_{ma})[>MnOH_2^+]$, where R is the dissolution rate (mol m^{-2} s^{-1}), $2\chi_{1/2}$ is the fraction of surface sites located at steps, $[>CO_3H]$ and $[>MnOH_2^+]$ are surface concentrations (mol m^{-2}), and k_{co}, k_{ca}, k_{mo}, and k_{ma} are the respective dissolution rate coefficients (s^{-1}) for the $>CO_3H$ and the $>MnOH_2^+$ surface species on obtuse and acute steps. We find $k_{co} = 2.7$ s^{-1}, $k_{ca} = 2.1 \times 10^{-1}$ s^{-1}, $k_{mo} = 4.1 \times 10^{-2}$ s^{-1}, $k_{ma} = 3.7 \times 10^{-2}$ s^{-1}, and $\chi_{1/2} = 0.015 \pm 0.005$. The rate coefficients quantify the net result of complex surface step processes, including double-kink initiation and single-kink propagation. We propose that the SSCM model may have general applicability for dissolution far from equilibrium of flat mineral surfaces of ionic crystals, at least those that dissolve by step retreat.

1. INTRODUCTION

Mineral dissolution rates are strongly related to surface chemistry and processes. Surface complexation modeling (SCM) provides a theoretical framework to relate aqueous solution chemistry to surface chemical processes (Dzombak and Morel, 1990; Goldberg, 1992; Stumm, 1992; Brown et al., 1999). The SCM approach identifies specific surficial chemical complexes formed between aqueous solution species and surficial hydroxyl and carbonate groups. This approach usually treats the surface as composed of one or two types of sites and implicitly omits any treatment of the effects of surface microtopography. SCM is successful in offering mechanistic chemical insights and in determining dissolution rate coefficients for specific surface chemical species (Stumm et al., 1985; Stumm and Wieland, 1990; Pokrovsky and Schott, 1999, 2002; Pokrovsky et al., 1999a; Duckworth and Martin, 2001).

A complementary theoretical approach, which stems from Burton-Cabrera-Frank theory (Burton et al., 1951), is based on morphologic and geometric models (GM) of dissolution (Jordan and Rammensee, 1996; Lasaga, 1998; Shiraki et al., 2000). Dissolution rates (mol $m^{-2}s^{-1}$) are calculated by dividing the rate of volume removal per unit area of surface by the material molar volume. For minerals exhibiting step retreat, the rate of volume removal is calculated by multiplying the step retreat velocity by the total step length occurring in a unit area and by the step height. Kink–kink annihilation (KKA), which is a molecular-level GM model of the physical processes underlying step retreat, successfully explains the dissolution of carbonates (Liang et al., 1996a,1996b; Teng et al., 1998; Jordan et al., 2001). In this model, double-kink sites initiate on steps, and single-kinks then propagate bidirectionally along the step until annihilation with another kink or step termination (Hirth and Lothe, 1982; Liang et al., 1996a,1996b; Teng et al., 1998; Jordan et al., 2001).

The SCM model, which is based primarily on a chemical interpretation of dissolution, and the GM model, in turn based primarily on a physical interpretation of dissolution, have successfully rationalized many observations of mineral dissolution reported in decades of literature. Application of these models, however, has been separate and exclusive. There is an intellectual need to consider integration of these successful models and thereby establish connections between physical and chemical theories of mineral dissolution.

In the current study, dissolution rates are measured for the $(10\bar{1}4)$ face of rhodochrosite ($MnCO_3$) under aqueous solution conditions far from equilibrium. Atomic force microscopy (AFM) observations of real-time morphologic changes of mineral surfaces are a widely employed contemporary experimental technique for the study of step retreat (Gratz et al., 1991; Bosbach and Rammensee, 1994; Liang et al., 1996a; Eggleston

* Author to whom correspondence should be addressed (smartin@deas.harvard.edu).

et al., 1998; Jordan and Rammensee, 1998; Teng et al., 1998; Shiraki et al., 2000). In the current work, a link is established between the microscopic morphologic processes observed by AFM at the mineral surface and the release rates of aqueous Mn^{2+} ion to solution as a consequence of dissolution. An analysis of the observations shows that the dissolution rates are proportional to the surface concentrations of specific chemical groups, as investigated by a surface complexation model (Van Cappellen et al., 1993). The time series of AFM observations are employed to determine rate coefficients for step retreat. These coefficients are rationalized by specific surface chemical species. Based upon the observations, we combine the SCM and GM models to propose a step-site surface complexation model (SSCM).

There are only a few studies on the kinetics of $MnCO_3$ growth (Sternbeck, 1997; Lebron and Suarez, 1999) and only one study on $MnCO_3$ dissolution rates (Pokrovsky and Schott, 2002). There is, however, an extensive literature on the growth and the dissolution of the isostructural mineral calcite ($CaCO_3$) (Plummer et al., 1979; Morse, 1983; Rickard and Sjoberg, 1983; Busenberg and Plummer, 1986; Schott et al., 1989; Compton and Pritchard, 1990; Hillner et al., 1992; MacInnis and Brantley, 1992; Stipp et al., 1994; Liang et al., 1996a,1996b; Booth et al., 1997; Hong et al., 1997; Liang and Baer, 1997; Teng and Dove, 1997; Jordan and Rammensee, 1998; Shiraki et al., 2000; Teng et al., 2000; Orme et al., 2001). The previous work on $CaCO_3$ greatly assists in the study of $MnCO_3$, which has important similarities in its behavior at the macroscopic and microscopic levels.

2. EXPERIMENTAL METHODOLOGY

2.1. Procedures

2.1.1. Surface Preparation

Crystals of rhodochrosite (sample #96030, Colorado) are obtained from the Harvard University Museum of Natural History. X-ray diffraction is performed with a Phillips X-ray diffractometer to confirm the identity of the mineral (trigonal, $R\bar{3}c$, $a = 4.7682$ Å, $c = 15.6354$ Å). Proton-induced X-ray emission spectroscopy (PIXE, Cambridge Accelerator for Materials Science [CAMS], Harvard University) is utilized to characterize the chemical composition of the surface region.

To prepare surfaces for the dissolution experiments, rhodochrosite crystals are cleaved along the (1014) plane (perfect cleavage) by sharply striking the butt of an aligned knife with a hammer. The cleaved sample is mounted on a steel puck by pressing the crystal into warmed dental modeling wax (Cavex, Holland) so that the edges of the crystal are covered with wax while the top is exposed for AFM imaging. A razor blade is used to scrape away excess wax. The mounted sample is immediately placed in the AFM fluid cell (Digital Instruments, Santa Barbara, CA) to minimize the potential exposure of the surface to airborne organic matter, dust, and other possible contaminants. A fresh sample is prepared in this manner for each experiment. After the experiment, the sample is imaged by a digital camera, and the geometric surface area (A) is calculated in Photoshop (Adobe Systems, San Jose, CA).

2.1.2. Preparation of Dissolution Liquor

Aqueous solutions of HCl or NaOH at several pH values are prepared on the day of each experiment by purging deionized water with argon (0.5 L min^{-1}) for 2 h. Impurities are removed from the argon by filtering through an in-line carbon dioxide trap (Alltech, Deerfield, IL) and an oxygen trap (Alltech). Freshly made HCl (EM OmniTrace grade) and NaOH (Aldrich, 99.998%) solutions are titrated into prepared water to create anoxic reservoir solutions at the desired pH. Ionic strength, arising from ions added to set pH, is less than 10 mM. These solutions are drawn into 60-mL plastic syringes and capped until use (within 6 h). Control studies, which monitor any possible changes in pH, confirm that the plastic syringes are impermeable to atmospheric CO_2 and O_2 during the timescale of our experiments.

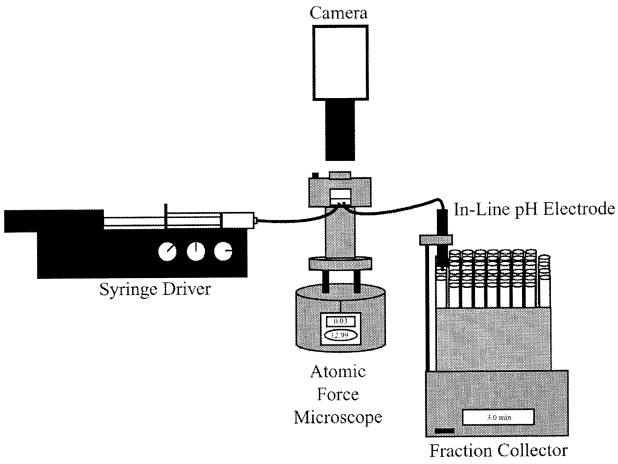

Fig. 1. Apparatus used in AFM/flow-through reactor experiments. A syringe pump drives solution (0.1 to 0.6 mL min^{-1}) via FEP tubing (low gas permeability) through the AFM fluid cell. The solution then travels through an in-line pH meter into test tubes in a fraction collector.

2.1.3. Simultaneous AFM/Flow-through Reactor Experiments

Figure 1 depicts the apparatus used in the simultaneous AFM/flow-through reactor experiments. The dissolution liquor is pumped (flow rate, q, of 0.1 to 0.6 mL min^{-1}) through the fluid cell via fluorinated ethylene propylene resin (FEP) tubing from a syringe driver (Orion Sage, Beverly, MA). The FEP tubing has low permeability to atmospheric gases. Syringes are switched up to three times during the course of a set of experiments to change the inlet solution pH. The effluent passes through a vertical flow pH electrode (Cole-Parmer, Vernon Hills, IL) and is collected by a fraction collector (Retriever 500; Isco, Lincoln, NE). Before analysis, samples having volumes equal to 5 min of flow are stored in the dark at 4°C in polypropylene test tubes for no more than 1 week. Samples are analyzed by graphite furnace atomic absorption spectroscopy (AAnalyst 300 atomic absorption spectrometer equipped with an HGA 850 graphite furnace attachment; Perkin-Elmer, Shelton, CT) to determine aqueous manganese concentration ([Mn]). Analytical standards read during analysis are within 10% of the known concentrations. Under our analytical conditions, the limit of detection for this technique is 2 nM.

While solutions are flowing through the fluid cell, the surface is imaged by AFM in contact mode (Nanoscope IIIa Multimode SPM; Digital Instruments) with oxide-sharpened Si_3N_4 nanoprobes (force constant of 0.12 N m^{-1}, radius of curvature of 5 to 40 nm, Digital Instruments). Images ranging in size from 1×1 to 120×120 μm^2 are scanned at 2 to 4 Hz. For analysis, only same direction scans (i.e., exclusively upscans or downscans) are used. At high pH, every other image in a series of images in the same scan direction is analyzed because only small changes in the position of steps occur between successive images.

2.2. Data Analysis

2.2.1. Macroscopic Dissolution Rates

Dissolution rates are calculated from the flux of aqueous manganese in the fluid cell effluent, as follows (Samson et al., 2000):

Table 1. Tabulated experimental conditions (flow rate, pH, and surface area) and results ($[Mn]_{ss}$, Q/K, R_{mac}, and R_{mic}) for AFM/flow-through reactor experiments. K_{sp} is taken from the MINEQL+ database (Schecher, 2001). Uncertainty estimates for R_{mic} and R_{mac} are provided in Fig. 5.

Experiment	pH	Flow Rate mL min^{-1}	Surface Area m^2	$[Mn]_{ss}$ (M)	Q/K_{sp}	R_{mac} (mol m^{-2}s^{-1})	R_{mic} (mol m^{-2}s^{-1})
1	2.4	0.20	7.3×10^{-6}	6.5×10^{-7}	1.9×10^{-14}	3.0×10^{-7}	2.0×10^{-7}
2	2.5	0.20	7.3×10^{-6}	5.6×10^{-7}	2.8×10^{-14}	2.5×10^{-7}	2.0×10^{-7}
3	3.3	0.50	9.0×10^{-6}	1.8×10^{-7}	8.0×10^{-14}	1.9×10^{-7}	1.0×10^{-7}
4	3.7	0.50	7.1×10^{-6}	1.4×10^{-7}	3.4×10^{-13}	1.5×10^{-7}	
5	3.9	0.50	9.0×10^{-6}	1.3×10^{-7}	7.5×10^{-13}	1.1×10^{-7}	
6	4.2	1.50	1.3×10^{-5}	3.8×10^{-8}	2.5×10^{-13}	9.7×10^{-8}	
7	4.7	0.50	9.0×10^{-6}	6.3×10^{-8}	7.0×10^{-12}	5.3×10^{-8}	
8	4.7	0.30	4.6×10^{-6}	5.5×10^{-8}	5.3×10^{-12}	5.0×10^{-8}	
9	4.8	0.50	9.0×10^{-6}	4.2×10^{-8}	5.3×10^{-12}	4.4×10^{-8}	
10	5.0	1.50	1.3×10^{-5}	5.3×10^{-8}	1.8×10^{-11}	6.0×10^{-8}	
11	5.2	0.30	4.6×10^{-6}	2.3×10^{-8}	1.0×10^{-11}	2.7×10^{-8}	
12	5.6	0.50	7.1×10^{-6}	3.1×10^{-8}	9.6×10^{-11}	3.1×10^{-8}	3×10^{-8}
13	5.6	0.30	9.9×10^{-6}	5.3×10^{-8}	3.2×10^{-10}	2.2×10^{-8}	
14	5.6	0.20	7.3×10^{-6}	1.3×10^{-7}	2.2×10^{-9}	2.3×10^{-8}	2×10^{-8}
15	5.8	0.30	4.6×10^{-6}	2.7×10^{-8}	1.0×10^{-10}	2.6×10^{-8}	
16	5.9	0.30	1.5×10^{-5}	3.8×10^{-8}	5.0×10^{-10}	1.2×10^{-8}	
17	6.5	0.60	1.3×10^{-5}	1.6×10^{-8}	9.4×10^{-10}	1.3×10^{-8}	
18	6.9	0.20	7.3×10^{-6}	6.4×10^{-8}	5.1×10^{-8}	1.2×10^{-8}	
19	7.5	0.30	1.5×10^{-5}	2.3×10^{-8}	2.7×10^{-8}	7.2×10^{-9}	
20	7.5	0.30	1.1×10^{-5}	2.6×10^{-8}	4.4×10^{-8}	1.0×10^{-8}	6×10^{-9}
21	7.8	0.60	1.3×10^{-5}	8.6×10^{-9}	7.6×10^{-9}	7.2×10^{-9}	
22	8.3	0.30	1.1×10^{-5}	2.1×10^{-8}	1.7×10^{-7}	4.9×10^{-9}	6×10^{-9}
23	8.5	0.30	1.5×10^{-5}	1.7×10^{-8}	1.5×10^{-7}	4.9×10^{-9}	
24	9.5	0.50	9.0×10^{-6}	3.6×10^{-9}	6.3×10^{-8}	3.5×10^{-9}	
25	10.3	0.50	7.1×10^{-6}	5.8×10^{-9}	6.1×10^{-7}	4.9×10^{-9}	4×10^{-9}
26	10.8	0.60	1.3×10^{-5}	3.8×10^{-9}	4.2×10^{-7}	3.0×10^{-9}	
27	11.0	0.30	1.1×10^{-5}	6.0×10^{-9}	1.1×10^{-6}	3.7×10^{-9}	

$$R_{mac} = \frac{\Delta[\mathrm{Mn}]\, q}{A}, \tag{1}$$

where R_{mac} (mol m^{-2} s^{-1}) is the macroscopic dissolution rate, Δ[Mn] is the difference in aqueous manganese concentration (M) between the influent and the effluent, q is the flow rate (L s^{-1}), and A is the geometric surface area (m^2) of the rhodochrosite sample. In our experiments, the inlet concentration is below the limit of detection (i.e., [Mn] < 2 nM). Depending on experimental conditions, effluent concentrations range from 4 to 650 nM.

2.2.2. Microscopic Dissolution Rates

A geometric analysis is employed to calculate the microscopic dissolution rates, R_{mic} (mol m^{-2} s^{-1}), by determining the volume of material removed from the surface. To carry out this calculation, we measure the average rate of step retreat (ν_{avg}, m s^{-1}) accompanying pit expansion on the mineral surface. The average rate of step retreat is then multiplied by the characteristic slope of the surface ($\Delta h/\Delta l$) to determine the microscopic dissolution rate, as follows (Shiraki et al., 2000):

$$R_{mic} = \frac{\nu_{avg}}{V_M}\left(\frac{\Delta h}{\Delta l}\right), \tag{2}$$

where V_M is the molar volume (m^3 mol^{-1}). The characteristic slope is an estimate of the product of the total step length occurring in a unit area and the step height. Eqn. 2 provides the formulation for the dissolution rate in the GM model, i.e., $R_{\mathrm{GM}} = R_{mic}$.

The term ν_{avg} is calculated by two alternate methods. In the first method the time-dependent displacements of the steps forming the perimeter of a rhombohedral pit are measured relative to a fixed point on the surface (e.g., a surface contaminant). Rhombohedral etch pits bounded by steps oriented in the $\langle 441\rangle$ and $\langle 481\rangle$ directions typically form on the 1014 surface of calcite (Hillner et al., 1992; Liang et al., 1996a), and the microtopographical features arising from dissolution on rhodochrosite are similar to those witnessed on calcite. The steps form obtuse or acute angles with the $(10\bar{1}4)$ surface (as labeled in Figs. 4 and 10) and as a result dissolution occurs anisotropically (Hillner et al., 1992; Teng et al., 1998): step retreat occurs more rapidly for the obtuse $\langle \bar{4}41\rangle$ and $\langle 48\bar{1}\rangle$ steps than for the acute $\langle 44\bar{1}\rangle$ and $\langle 18\bar{1}\rangle$ steps (Liang and Baer, 1997; Jordan and Rammensee, 1998; Teng et al., 1998). The ν_{avg} term is determined by the arithmetic average of the obtuse and acute step retreat rates, ν_o and ν_a.

The second method for determining ν_{avg} follows from the time-dependent changes in the lateral dimensions of pits, as observed in successive images captured in the same scan direction. The calculation is as follows:

$$\nu_{avg} = \frac{1}{2}\frac{1}{2}\frac{1}{\tau}\frac{\sum_{i}^{2(N-1)} \Delta x_i}{2(N-1)}, \tag{3}$$

where Δx_i is the change in a lateral pit dimension, τ is the acquisition time for the image, and N is the number of images in the series. The two factors of one-half arise from the movement of two opposing walls (i.e., two retreating steps simultaneously measured) and the doubling of acquisition time associated with using only same-direction scans. The iterator runs from 1 to $2(N-1)$ because there are two lateral dimensions characterizing the rhombohedral pit in each image. This second method omits treatment of anisotropic step retreat velocity among the pit walls because the average step retreat rate of two opposing walls is measured. As a result of this disadvantage, this method is used only when a fixed reference point suitable for the first method is absent. In all cases where both analysis methods are possible, the ν_{avg} results agree within experimental uncertainty.

For experiments that do not yield images suitable for either method of analysis, R_{mic} is not calculated, although R_{mac} is still measured from the [Mn] in the effluent (Eqn. 1). As revealed in Table 1, in our work there are 8 successful determinations of R_{mic} in 27 attempts. In the 19 failed attempts, no surface changes are observed in ten cases. Presumably, step retreat is still the dominant dissolution mechanism but is not observed in our imaging. The absence of pits in the imaged area may

be due to the lack of crystal defects in this region of the surface. The other nine failed attempts arise from the observed dissolution not occurring via a mechanism of the expansion of regular rhombohedral pits. In these cases, the surface is characterized by ragged steps and pits with ragged or curved edges. Our approach to image analysis, which is based on calculating ν_{avg} by one of the two methods described above, is not applicable when irregular pits occur with curved or ragged steps, as in the last nine cases. Other workers have analyzed sections of calcite surfaces, when dominated by ragged steps from the intersection of pits, and have concluded that dissolution rates are similar to regions dominated by rhombohedral pit expansion (Jordan and Rammensee, 1998). The macroscopic dissolution rates from these 19 trials are consistent with the values interpolated from the eight trials for which both microscopic and macroscopic data are available.

In addition to ν_{avg}, evaluation of R_{mic} by Eqn. 2 also requires a numerical value of $\Delta h/\Delta l$. The characteristic slope ($\Delta h/\Delta l$) is calculated for a large plane-fitted scan (40×40 μm^2 or greater) by subtracting the z-height of each point in the 512×512 matrix (x,y) of height values from its eight closest neighbors to obtain $(\Delta h_i)_{x,y}$ for $i = 1$ to 8, by then dividing each $(\Delta h_i)_{x,y}$ by the lateral extent $(\Delta l_i)_{x,y}$ (e.g., relative length of 1 for lateral positions and $\sqrt{2}$ for diagonal positions), and by then taking the maximum value among these eight difference values to obtain $(\Delta h/\Delta l)_{x,y}$ (Shiraki et al., 2000). The arithmetic average of all elements of the resulting matrix (510×510) is defined as the characteristic slope of the surface, $\Delta h/\Delta l$. The algorithm is implemented in *Mathematica* (Wolfram Research, Champaign, IL).

There are several limitations inherent in our approach to calculating R_{mic} (viz. Eqn. 2), especially in regard to $\Delta h/\Delta l$. First, the approach does implicitly assume that dissolution occurs dominantly at steps, albeit such a dissolution mechanism is generally supported by both experimental and theoretical work (Burton et al., 1951; Gratz et al., 1991). Second, the use of $\Delta h/\Delta l$ to calculate dissolution rates assumes that the slope associated with a point on the surface is due to a step. This assumption is reasonable for clean, nearly flat surfaces of a single crystal face, such as the rhodochrosite surface in the present study. Third, the large scans used to calculate $\Delta h/\Delta l$ have limited lateral resolution, with one pixel representing 100 to 200 nm^2. Thus, a pixel is the average height of an area much larger than the scale of an atomic step, while $\Delta h/\Delta l$ employed in Eqn. 2 is predicated on atomic level measurements. So long as the subpixel variance in height is small (i.e., a smooth surface), then the calculation of $\Delta h/\Delta l$ from pixel height values is accurate and also independent of the surface area corresponding to a single pixel. The condition of a smooth surface is confirmed us by observing that the surface is flat at smaller scan sizes.

2.2.3. Equilibrium Surface Complexation Modeling

Following from earlier titration data (Charlet et al., 1990), Van Cappellen et al. (1993) offer a surface complexation model for rhodochrosite. Specifically, they provide the formation constants for surficial $>CO_3H$ and $>MnOH$ groups in a constant capacitance model (Stumm, 1992). Due to the high capacitance of carbonates (Charlet et al., 1990; Van Cappellen et al., 1993; Pokrovsky et al., 1999b; Pokrovsky and Schott, 2002), we estimate $\kappa = 15$ F m^{-2} for our ionic strength range. Formation constants of aqueous species are provided in a critically reviewed database within MINEQL+ (Environmental Research Software, Hallowell, ME) (Schecher, 2001). Employing MINEQL+, we model the equilibrium surface speciation of rhodochrosite for the aqueous chemical conditions inside the AFM fluid cell.

3. RESULTS

Rhodochrosite samples are characterized to confirm their mineralogy and to quantify contamination. The X-ray diffraction analysis identifies the material as well-crystalline rhodochrosite with no other detectable phases present. The PIXE results of the surface chemical constituents are provided in Table 2. The sample has a Mn purity of 99.59%, with Zn and Ca impurities of 0.20% and 0.17%, respectively. Other common contaminants, including Cd, Fe, Ni, and Sr, are present at levels below the minimum detection limit of PIXE (Table 2).

Table 2. Elemental composition of rhodochrosite as determined by PIXE analysis.

Element	Percentage of Cation
Ca	0.17
Cd	< 0.03
Fe	< 0.4
Mn	99.59
Ni	< 0.003
Sr	< 0.007
Zn	0.2

Figure 2 shows a typical time course profile of pH and [Mn] during an experiment. pH rapidly obtains a steady value, both at the start of the experiment and after a change in influent. Except for an initial transient at the beginning of the experiment, [Mn] rapidly reaches a steady-state concentration for each pH value. The initial transient possibly arises from the dissolution of high-energy sites created by cleaving the mineral. Steady-state dissolution rates for a selected pH value are calculated from the average [Mn] at steady-state, according to Eqn. 1 The results from 27 experimental trials are summarized in Table 1.

Figure 3 shows a typical AFM micrograph (50×50 μm^2) of

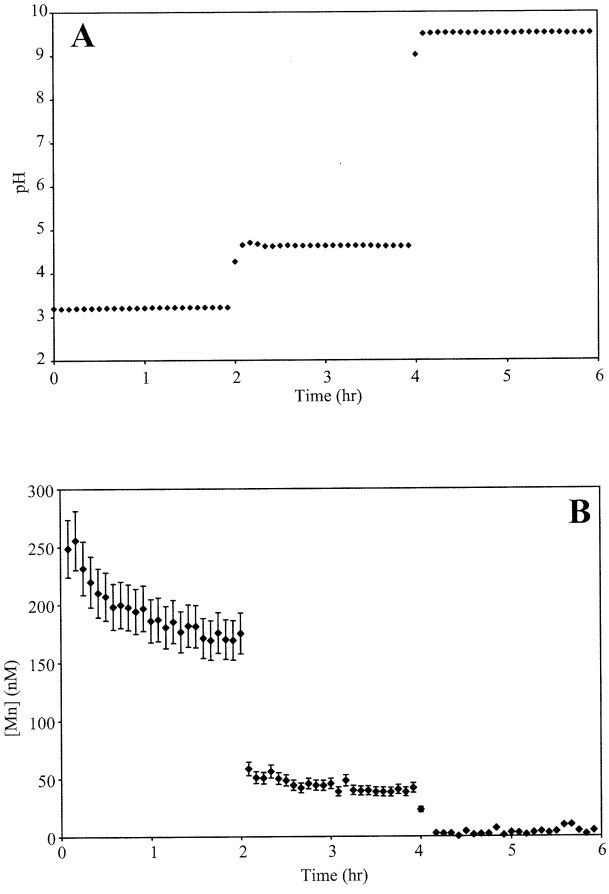

Fig. 2. The profile of (A) pH and (B) [Mn] throughout the course of a set of experiments. The flow rate during this experiment is 0.5 mL min^{-1}. The dissolution rate (mol $m^{-2}s^{-1}$) is given by Eqn. 1.

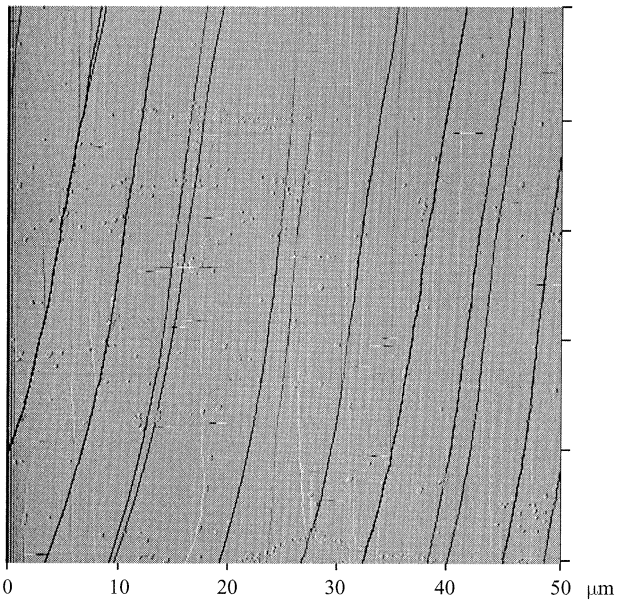

Fig. 3. AFM micrograph of the surface shortly after exposure to an aqueous solution (pH = 5.6). The average height of steps is 5.5 nm.

the cleaved rhodochrosite surface shortly after exposure to solution (pH = 5.6). The surface has a *z*-height of 50 nm and is characterized by parallel terraces of ~3 μm lateral extent punctuated by steps. The average height of these steps is 5.5 nm, which is about 20 times the estimated height of a rhodochrosite monolayer oriented perpendicular to the $(10\bar{1}4)$ face. At the end of the experiments (typically 8 h), etch pits are visible (not shown). However, no other significant changes in morphology are evident at the length scale characteristic of Figure 3.

In time, pits begin to appear in the terrace regions of Figure 3. A time series of AFM micrographs (Fig. 4) at higher resolution (1.25×1.25 μm^2) reveals the appearance and the expansion of an etch pit on the $(10\bar{1}4)$ face of rhodochrosite at pH = 3.6. The depth of the flat-bottomed pit is 4 nm (~14 monolayer heights) and does not increase during imaging. In general, pits are either shallow and flat-bottomed or deep and pointed. This aspect of morphology depends on the crystal defect, which is the precursor to the etch core (MacInnis and Brantley, 1992). The internal angles (77° and 103°) of the etch pit arise from intersection of the $\langle\bar{4}41\rangle$ and $\langle 48\bar{1}\rangle$ crystallographic vectors, as verified by us in the software package Crystal Office (Atomic Softek, Ontario, Hamilton, Ontario).

The well-formed rhombohedral morphology is observed at pH = 3.7, 7.5, 8.3, and 10.3. At pH = 5.6, rounding of one of the obtuse angles is apparent. Pits with a similar rounding of one obtuse angle are reported for calcite at pH values near neutral (Stipp et al., 1994; Jordan et al., 2001). For pH $\leq$ 2.5, we observe slight rounding of edges and distortion of internal angles, which may indicate the onset of a transition to a new pit morphology at low pH. By way of comparison, a change in pit morphology is known for magnesite [$MgCO_3$] for pH $\leq$ 4 at elevated temperature (Jordan et al., 2001). Magnesite and rhodochrosite are isostructural.

Several small surface contaminants (~125 nm in diameter) are also present in the micrographs in Figure 4. These contaminants do not change during the course of the experiment and serve as convenient reference points for image analysis. Steps move under these contaminants without any apparent alteration of pit morphology from a regular rhombohedron (e.g., Figs. 4A–D), suggesting no strong surficial interaction.

Micrographs such as those shown in Figure 4 are analyzed by the methods provided for in Eqns. 2 and 3 to obtain $\Delta h/\Delta l$ from height images and ν_a, ν_o, and ν_{avg} from deflection images over a range of pH values (Table 3). $\Delta h/\Delta l$ shows no clear dependence on pH, with a mean value of 0.03 ± 0.01. This mean value agrees well with the pH-independent value for calcite of 0.026 ± 0.015 (Shiraki et al., 2000). The dissolution rates determined from these microscopic observations (Eqn. 2) are provided in Table 1, and they are in excellent agreement

Table 3. $\Delta h/\Delta l$, ν_a, ν_o, and ν_{avg} (nm s^{-1}) over a range of pH values. The number of measurements included in the calculation of the reported parameter is shown in parentheses. The mean of $\Delta h/\Delta l$ values is 0.03 ± 0.01.

pH	$\Delta h/\Delta l$	$n_{\Delta h/\Delta l}$	ν_a	ν_o	ν_{avg}	$n_{\nu avg}$
2.4	—	(0)	$4 \pm 1 \times 10^{-2}$	$3.2 \pm 0.3 \times 10^{-1}$	$1.8 \pm 0.4 \times 10^{-1}$	(8)
2.5	—	(0)	$3.4 \pm 0.7 \times 10^{-2}$	$3.2 \pm 0.6 \times 10^{-1}$	$1.9 \pm 0.7 \times 10^{-1}$	(13)
3.7	0.03	(5)	$3 \pm 1 \times 10^{-2}$	$1.5 \pm 0.4 \times 10^{-1}$	$9.2 \pm 0.9 \times 10^{-2}$	(20)
3.9	0.05	(9)	—	—	—	(0)
4.7	0.06	(9)	—	—	—	(0)
4.8	0.02	(5)	—	—	—	(0)
5.2	0.04	(4)	—	—	—	(0)
5.6	0.03	(7)	$1.5 \pm 0.9 \times 10^{-2}$	$3.5 \pm 0.7 \times 10^{-2}$	$2 \pm 1 \times 10^{-2}$	(37)
5.8	0.03	(2)	—	—	—	(0)
5.9	0.01	(4)	—	—	—	(0)
6.5	0.01	(4)	—	—	—	(0)
6.9	0.05	(7)	—	—	—	(0)
7.5	0.02	(10)	—	—	$5 \pm 1 \times 10^{-3}$	(12)
7.8	0.03	(4)	—	—	—	(0)
8.3	0.03	(5)	$5 \pm 4 \times 10^{-3}$	$6 \pm 2 \times 10^{-3}$	$5 \pm 3 \times 10^{-3}$	(15)
8.5	0.05	(2)	—	—	—	(0)
10.3	0.04	(7)	$3 \pm 2 \times 10^{-3}$	$4 \pm 2 \times 10^{-3}$	$4 \pm 2 \times 10^{-3}$	(14)
10.8	0.02	(7)	—	—	—	(0)
11.0	0.03	(4)	—	—	—	(0)

with the values determined from the macroscopic observations (Eqn. 1).

Table 1 summarizes the conditions (i.e., pH, surface area, $[Mn]_{ss}$, and estimated Q/K_{sp}) and the results (i.e., R_{mic} and R_{mac}) of each AFM/flow-through experiment. Because the inlet solutions are purged with argon and because CO_2-diffusion through the FEP tubing walls is negligible on the timescale of the experiments, total carbonate (i.e., $[CO_3]_{total}$ is the sum of $[H_2CO_3]$, $[HCO_3^-]$, and $[CO_3^{2-}]$) equals $[Mn]_{ss}$ (Stumm and Morgan, 1996). In this case, the rhodochrosite saturation ratio (Q/K_{sp}) is calculable and is less than 10^{-6}, indicating the reaction is far from equilibrium for all experiments. Results shown in Table 1 indicate that the dissolution rates do not vary with the flow rate, which suggests dissolution is surface-controlled for our apparatus conditions (Shiraki et al., 2000). The log values of the dissolution rates reported in Table 1 are plotted against pH in Figure 5. Open and closed markers show $\log[R_{mic}]$ and $\log[R_{mac}]$, respectively. The good agreement between R_{mic} and R_{mac} indicates that the AFM observations are successfully viewing the representative surface features responsible for most of the dissolution.

The results of surface complexation modeling of rhodochrosite are shown in Figure 6. $[CO_3]_{total}$ and $[Mn^{2+}]$ used in the model are based on the mean concentrations for all experimental trials. Figure 6A shows the speciation of manganese hydroxyl surface sites as a function of pH. The dominant surface species from pH = 2 to 11 is $>MnOH_2^+$, whose concentration is nearly constant over this pH range. $[>MnOH]$ is significant at high pH. $[>MnO^-]$, $[>MnHCO_3^+]$, and $[>MnCO_3]$ are negligible at all pH values. Figure 6B shows the speciation of surficial carbonate groups from pH = 2 to 11. The $>CO_3^-$ species dominates over most of the pH range. However, at low pH the protonated species $>CO_3H$ is significant. The dominant species modeled here are consistent with those determined for the $(10\bar{1}4)$ face of calcite by high resolution X-ray reflectivity (Fenter et al., 2000). Figure 6C shows the modeled surface charge as a function of pH. The pH_{zpc}, which depends on $[CO_3]_{total}$, is 7.5 for our reactor conditions. This value, which is slightly higher than reported by Van Cappellen et al. (1993), arises from the low $[CO_3]_{total}$ in our system.

4. DISCUSSION

4.1. Mechanistic Model of Dissolution

Carbonate dissolution far from equilibrium is often formulated as follows (Busenberg and Plummer, 1986; Chou et al., 1989):

$$MCO_3(s) + H^+ \rightarrow M^{2+} + HCO_3^- \quad (4)$$

$$MCO_3(s) + H_2O \rightarrow M^{2+} + HCO_3^- + OH^- \quad (5)$$

Although stoichiometrically equivalent in water, Eqns. 4 and 5 convey mechanistic distinction: proton-promoted (Eqn. 4) and unassisted hydrolysis (Eqn. 5) are distinct mechanistic pathways for dissolution. The relative contribution of each pathway to the overall dissolution rate depends strongly on pH. Rate laws, developed for calcium, magnesium, strontium, and iron carbonates (Busenberg and Plummer, 1986; Chou et al., 1989; Dresel, 1989), provide insight into reaction pathways by quantitatively relating the dissolution of carbonates to concentrations of aqueous species. Rate laws formulated in this manner are often called mechanistic models (MM) (Busenberg and Plummer, 1986), and they are distinct from the SCM and GM models.

To formulate a MM for rhodochrosite, we fit the data in Table 1 to the concentrations of reactant species, viz. H^+ and H_2O. An empirical model based on this approach yields

$$R_{MM} = 10^{-4.93}[H^+]^{0.5} + 10^{-8.45}[H_2O] \quad (6)$$

where $[H_2O] \equiv 1$. The dissolution rate law provided in Eqn. 6 depends on the square root of the proton concentration (Eqn. 4) and a constant water-promoted rate (Eqn. 5). The model, which is plotted as a dashed line in Figure 5, shows good agreement of R_{mic} and R_{mac} with R_{MM} over a wide pH range, though the model fails for pH $\leq$ 3. A change in dissolution mechanism from proton-promoted to unassisted hydrolysis is implicated in the inflection point apparent in Figure 5 at pH = 7. The advantage of MM, as opposed to SCM and GM, is the relative ease of formulation of rate laws from macroscopic dissolution data and aqueous species concentrations. The disadvantage is the absence of scientific insight at the molecular level and the consequent breakdown of the empirical rate laws when dissolution occurs outside the range of calibration (e.g., highly acidic pH).

4.2. SCM of Dissolution

To gain insight into reactions occurring at the mineral surface, dissolution rates are related to the concentration of surface species through the use of a SCM (Stumm et al., 1985; Stumm and Wieland, 1990; Pokrovsky and Schott, 1999, 2002; Pokrovsky et al., 1999a; Duckworth and Martin, 2001). In previous work on proton-promoted dissolution of metal oxides, the dissolution rate has been related to the surface concentration of metal hydroxyl groups, as follows (Stumm and Furrer, 1987):

$$R_{SCM} = k' [>MOH_2^+]^n \quad (7)$$

where $[>MOH_2^+]$ is the concentration of protonated surface metal hydroxyl groups (mol m^{-2}), k' is the dissolution rate coefficient (the prime indicates k is a lumped parameter; cf. Eqn. 11), and the order of the reaction (n) is typically a positive integer. In analogy, we consider carbonate dissolution. The rate law is modified to account for the presence of both metal hydroxyl (m) and carbonate (c) groups present on the mineral surface, any one or several of which could contribute to the observed dissolution. Previous workers have implicated $>CO_3H$ and $>MnOH_2^+$ as the species active in dissolution (Pokrovsky et al., 1999a,1999b; Pokrovsky and Schott, 2002). The SCM rate law is then formulated as follows:

$$R_{SCM} = k'_m [>MnOH_2^+]^{n_m} + k'_c[>CO_3H]^{n_c} \quad (8)$$

Surface concentrations under the range of experimental conditions are provided in Figure 6.

The reaction orders and the rate coefficients in Eqn. 8 are determined by a log-log plot (Fig. 7) of the dissolution rate vs. surface species concentration, in the regime in which one surface species dominates, as follows:

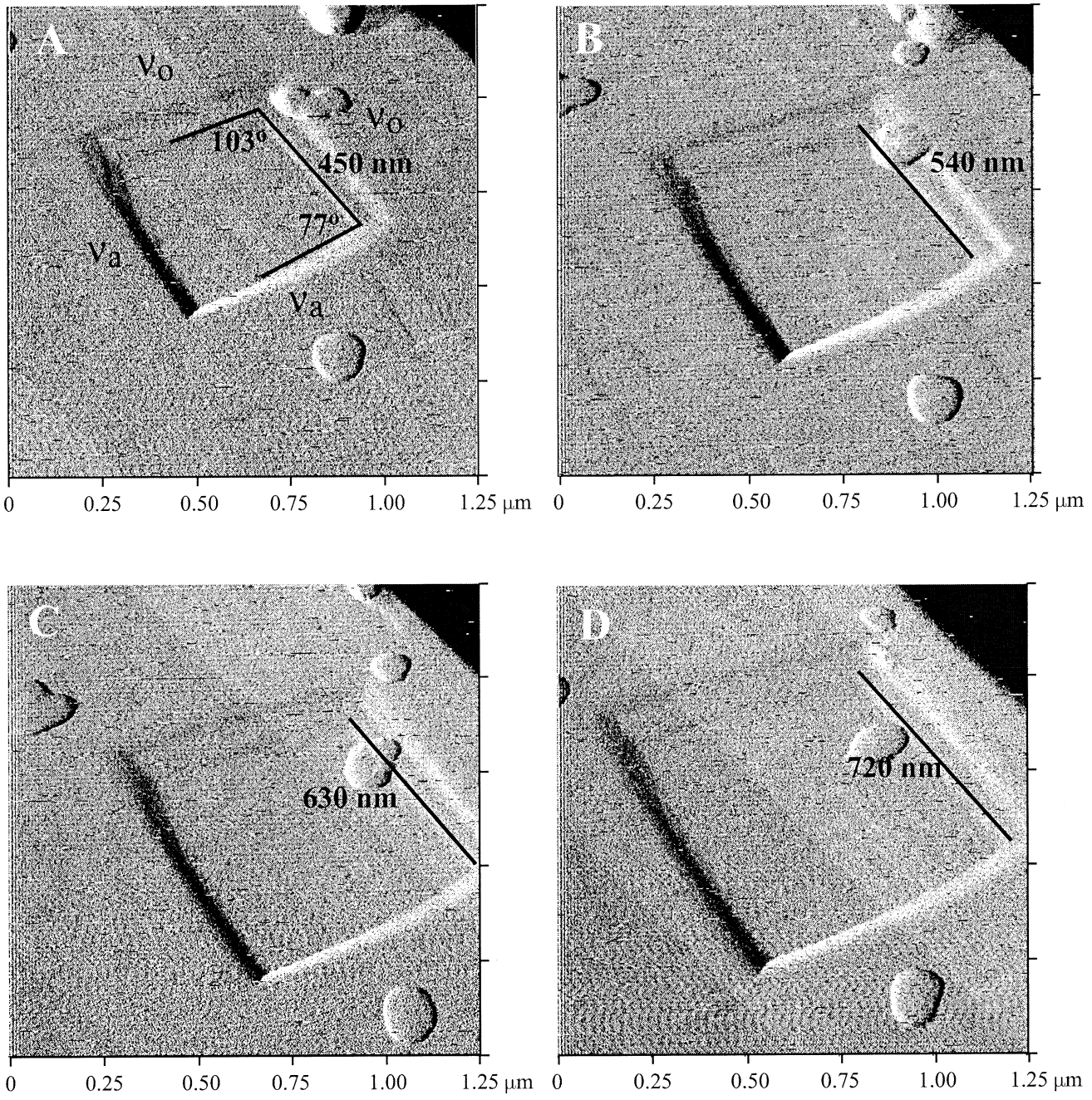

Fig. 4. Time series of deflection mode AFM images of an etch pits on the $(10\bar{1}4)$ face of rhodochrosite at pH = 3.6. The pit is bordered by crystallographically equivalent $\langle 441 \rangle$ and $\langle 48\bar{1} \rangle$ steps, i.e., a rhombohedral pit with internal angles of 77° and 103°. The pit expands at a rate of 90 nm per image, and there are 512 s between micrographs. Etch pit depth is 4 nm in these images.

$$\text{acidic} \quad \log[R_{SCM}] = n_c \text{Log}[{>}CO_3H] + \text{Log}[k_c'] \quad (9a)$$

$$\text{alkaline} \quad \log[R_{SCM}] = n_m \text{Log}[{>}MnOH_2^+] + \text{Log}[k_m']. \quad (9b)$$

Dissolution rates for pH < 7 (acidic regime) are plotted against $[{>}CO_3H]$, whereas for pH > 7 (alkaline regime), dissolution rates are plotted against $[{>}MnOH_2^+]$. Best-fit lines yield y-intercepts of $k_c' = 2.3 \pm 0.6 \times 10^{-2}$ s^{-1} and $k_m' = 6.8 \pm 0.2 \times 10^{-4}$ s^{-1}. The slopes are unity, indicating reaction orders of $n_m = 1$ and $n_c = 1$. Other candidate combinations of dissolution rates (Table 1) vs. model aqueous surface concentrations (Fig. 6) over varying pH do not succeed in providing linear relationships, in contrast to the linear relationships of unity slope for $[{>}CO_3H]$ and $[{>}MnOH_2^+]$.

The unity reaction orders are consistent with findings for other minerals, whose reaction orders are typically integer

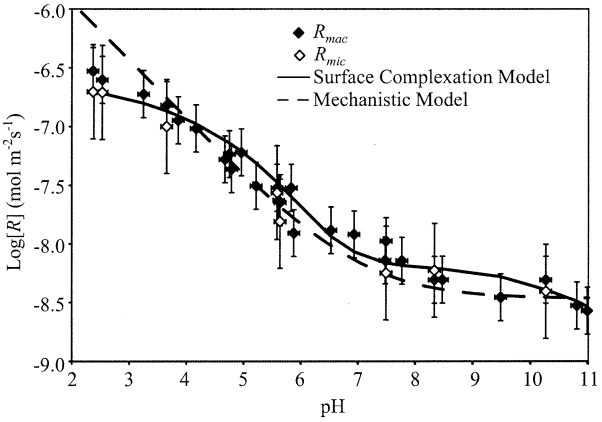

Fig. 5. Dissolution rate of rhodochrosite as a function of pH. Open and closed markers are microscopic (R_{mic}) and macroscopic (R_{mac}) dissolution rates, respectively. The dashed line shows the results of a MM relating the pH-dependent dissolution rate to the concentrations of aqueous species (M). The solid line shows the results of a surface complexation model relating the pH-dependent dissolution rate to the concentrations of surface species (mol m^{-2}). (In the figure, all open markers are visible to the reader.)

values (Stumm and Furrer, 1987). Our dissolution rates agree well with those measured by Pokrovsky and Schott (2002) for rhodochrosite at pH $<$ 8, but for pH $>$ 8 their rates are significantly slower. As a consequence, they report reaction orders of $n_c = 2$ and $n_m \cong 4.5$. These differences in reported dissolution behaviors for rhodochrosite are possibly explained by noting that by Pokrovsky and Schott employ powders having multiple crystal faces and edges exposed, in contrast to the current study's use of a large single crystal having only the $(10\bar{1}4)$ face exposed.

Applying the determined parameter values to Eqn. 8, we obtain the SCM rate law, as follows:

$$R_{SCM} = 10^{-3.2}[>MnOH_2^+] + 10^{-1.6}[>CO_3H] \qquad (10)$$

This equation is plotted as the solid line in Figure 5 and provides good agreement of R_{mic} and R_{mac} with R_{SCM}. The rate

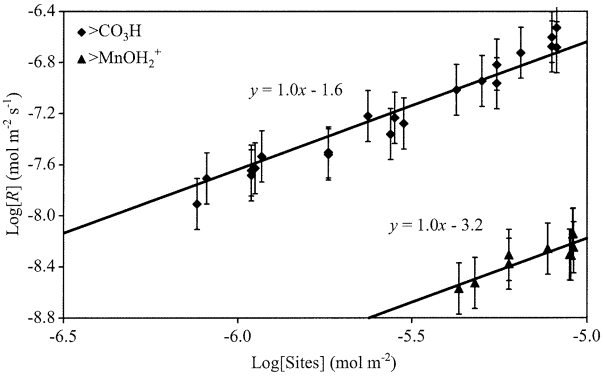

Fig. 7. Log–log plot of the dissolution rate vs. the surface concentration of $>CO_3H$ sites in the acidic dissolution regime (pH $<$ 7) and vs. the surface concentration of $>MnOH_2^+$ sites in the alkaline dissolution regimes (pH $>$ 7). Lines are empirical fits. For the acidic regime, $R^2 = 0.91$; for the alkaline regime, $R^2 = 0.81$.

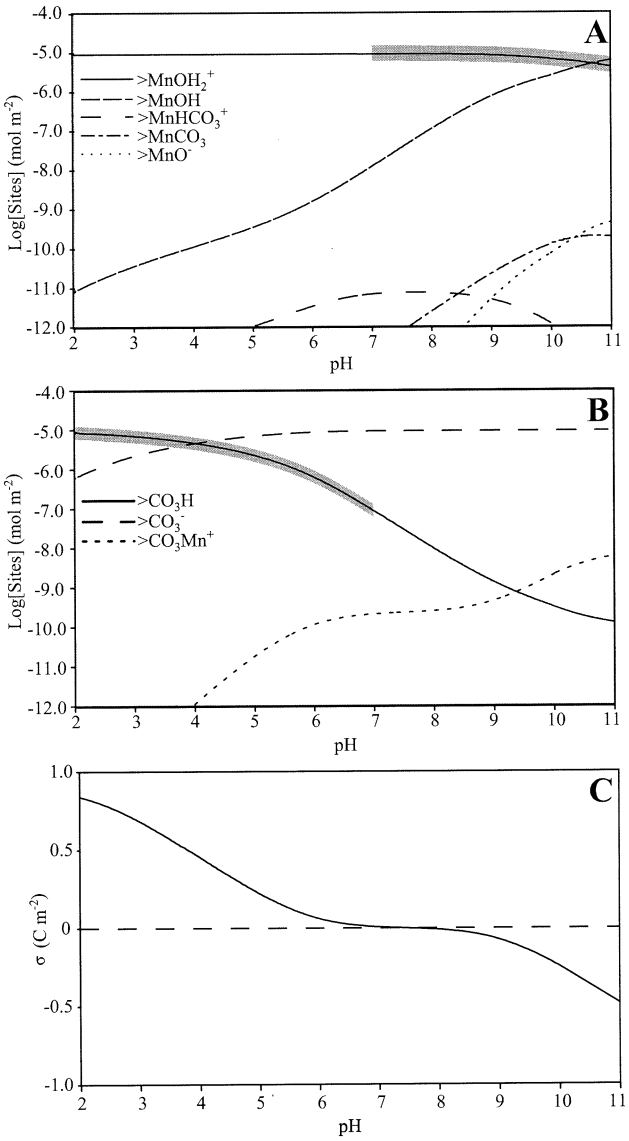

Fig. 6. (A) Modeled speciation of surficial manganese hydroxyl groups modeled speciation of (B) surficial carboxylate groups, and (C) net surface charge on rhodochrosite as a function of pH. Calculations are based on the mean aqueous concentrations of $[Mn]_{ss}$ and $[CO_3]_{total}$ and the mean surface area for all experiments. The shaded areas indicate the dominant surface chemical species implicated as active in dissolution (see text). Conditions: $[Mn]_{ss} = 9.8 \times 10^{-8}$ M, $[CO_3]_{total} = 9.8 \times 10^{-8}$ M, specific surface area $= 4.9 \times 10^{-2}$ m^2 L^{-1}, site density $= 9.2 \times 10^{-6}$ mol m^{-2}, $\kappa = 15$ F m^{-2}. Ionic strength is calculated from the concentration of each species (including pH) at each point. Formation constants for the surface species are from Van Cappellen et al. (1993); site density is taken from Pokrovsky and Schott (2002); and the aqueous formation constants are from the MINEQL+ database (Schecher, 2001).

equation shows first-order dependence on both $[>CO_3H]$ and $[>MnOH_2^+]$, each of which depends on pH.

The SCM model improves on the MM model by decoupling adsorption and dissolution, which are lumped together in Eqns. 4 and 5, into equilibrium adsorption of specific chemical surface species and a first-order dissolution rate law for each species. Due to the treatment of adsorption, the SCM model

performs well over the entire pH range, in contrast to the breakdown of the MM model at low pH. Although the SCM model successfully accounts for the variance in the dissolution data (i.e., a good model fit), the model faces conceptual limitations. Primarily, it fails to provide information on the morphologic and the geometric mechanisms active during dissolution and observable in the AFM.

4.3. SSCM of Dissolution

Because the AFM observations and the microscopic rate calculations show that the dissolution rate is explained from the movement of steps, we conclude the SCM active sites for rhodochrosite are steps. It then follows that the dissolution process is driven by the chemical species $>CO_3H$ and $>MnOH_2^+$ located at steps, and only those surface chemical species at steps are dissolution active. The revised rate law for the SSCM of dissolution is expressed as follows:

$$R_{SCM} = k'_m[>MnOH_2^+] + k'_c[>CO_3H]$$
$$= k_m\chi_m[>MnOH_2^+] + k_c\chi_c[>CO_3H] = R_{SSCM} \quad (11)$$

where χ is the fraction of active sites on the surface and k is the rate coefficient. In the case of rhodochrosite, because dissolution occurs by the mechanism of step retreat, χ is a proportionality factor relating the chemical species concentration at steps to the average concentration across the surface. The good agreement of R_{mic} and R_{mac} with R_{SCM} necessarily requires that the steps have surface species concentrations proportional to the average surface speciation. Previous reports (e.g., Stumm and Wieland, 1990) have also remarked that only certain locations on surfaces are active; however, no quantitative information on the value of χ or the physicochemical nature of active sites is reported.

We connect the SCM and GM models by requiring equality among all dissolution rate laws (Eqns. 1, 2, and 11). Specifically, setting $R_{GM} = R_{SCM}$, we obtain

$$\text{acidic} \quad \nu_{avg} = k_c\chi_c V_M\left(\frac{\Delta l}{\Delta h}\right)[>CO_3H] \quad (12a)$$

$$\text{alkaline} \quad \nu_{avg} = k_m\chi_m V_M\left(\frac{\Delta l}{\Delta h}\right)[>MnOH_2^+] \quad (12b)$$

for $n_c = 1$ and $n_m = 1$. Because k_c, k_m, χ_c, χ_m, V_M, and $\Delta h/\Delta l$ are constant, the average step velocity is proportional to the surface concentration of protonated carbonate sites in the acidic regime and to the surface concentration of protonated manganese hydroxyl sites in the alkaline regime. This analysis is then testable by plotting ν_{avg} vs. $[>CO_3H]$ and vs. $[>MnOH_2^+]$ in the acidic and the alkaline regimes, respectively (Fig. 8). Lines having slopes of $k_c\chi_c V_M(\Delta l/\Delta h)$ and $k_m\chi_m V_M(\Delta l/\Delta h)$ are obtained. In the acidic regime the slope yields $\Delta h/\Delta l = 0.032$ when $V_M = 3.1 \times 10^{-5}$ m^3 mol^{-1} and $k'_c = k_c\chi_c = 10^{-1.6}$ s^{-1}. In the alkaline regime we obtain $\Delta h/\Delta l = 0.035$ when $k'_m = k_m\chi_m = 10^{-3.2}$ s^{-1}. (In Fig. 8B, much of the y-axis is experimentally inaccessible at the lower values of ν_{avg} because the rate of step retreat is too slow to determine reliably by in situ AFM imaging.) An important observation is that the $\Delta h/\Delta l$ values determined by this independent kinetic analysis agree with the value as determined from our analysis of AFM micrographs (i.e., 0.03 ± 0.01) and also with the literature value of 0.026 ± 0.15, as cited for calcite (Shiraki et al., 2000). The relationships expressed in Eqn. 12 are thus confirmed by Figure 8.

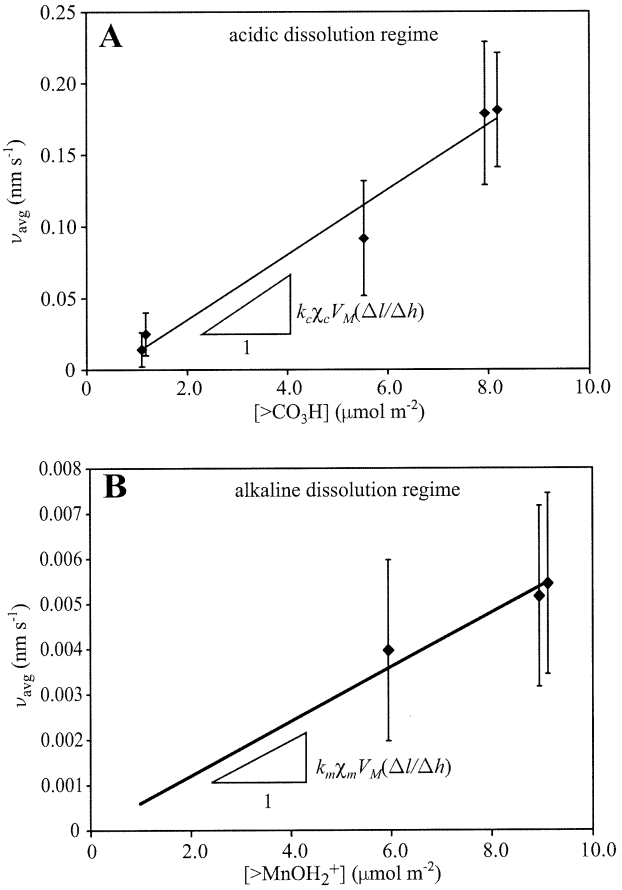

Fig. 8. (A) Average step velocity (ν_{avg}) vs. surface concentration of $>CO_3H$ sites in the acidic dissolution regime (pH < 7) and (B) average step velocity (ν_{avg}) vs. surface concentration of $>MnOH_2^+$ sites in the acidic dissolution regime (pH > 7).

4.3.1. *Determining the Products $k_{co}\chi_{co}$, $k_{ca}\chi_{ca}$, $k_{mo}\chi_{mo}$, and $k_{ma}\chi_{ma}$*

To gain further insight into the surface processes, we break the lumped parameter ν_{avg} into the individual contributions by the obtuse and the acute steps, ν_o and ν_a. Following from Eqn. 12 the relationship for the acidic dissolution regime is

$$\text{obtuse} \quad \nu_o = k_{co}\chi_{co} V_M\left(\frac{\Delta l}{\Delta h}\right)[>CO_3H] \quad (13a)$$

$$\text{acute} \quad \nu_a = k_{ca}\chi_{ca} V_M\left(\frac{\Delta l}{\Delta h}\right)[>CO_3H] \quad (13b)$$

where k_{co} and k_{ca} are the rate coefficients for the dissolution of the obtuse and the acute steps, respectively. Similar to Eqn. 12 and Figure 8, the analysis leading to Eqn. 13 yields linear relationships (Fig. 9A) when ν_o and ν_a are plotted against $[>CO_3H]$ in the acidic regime. We obtain $k_{co}\chi_{co} = 4.1 \times 10^{-2}$

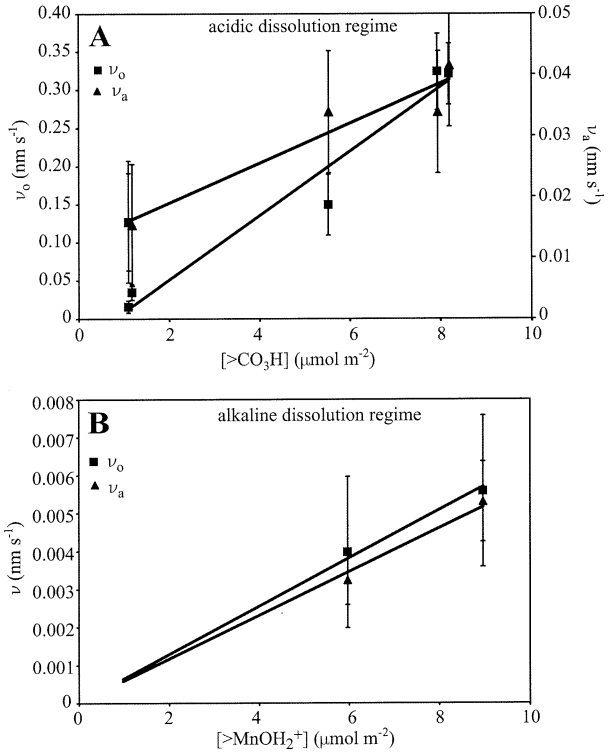

Fig. 9. (A) Obtuse (ν_o) and acute (ν_a) step velocity vs. surface concentration of [$>CO_3H$] sites in the acidic dissolution regime (pH $<$ 7) and (B) obtuse (ν_o) and acute (ν_a) step velocity vs. surface concentration of [$>MnOH_2^+$] sites in the alkaline dissolution regime (pH $>$ 7).

s^{-1} and $k_{ca}\chi_{ca} = 3.2 \times 10^{-3}\ s^{-1}$ for $\Delta h/\Delta l = 0.03$. A similar analysis for ν_o and ν_a vs. [$>MnOH_2^+$] in the alkaline regime yields $k_{mo}\chi_{mo} = 6.1 \times 10^{-4}\ s^{-1}$ and $k_{ma}\chi_{ma} = 5.6 \times 10^{-4}\ s^{-1}$.

4.3.2. Determining χ_{co},χ_{ca}, χ_{mo}, χ_{ma}, and k_{co}, k_{ca}, k_{mo}, k_{ma}

To estimate χ_{co}, χ_{ca},χ_{mo}, andχ_{ma}, we make two assumptions: (1) per unit area, step site chemical species concentrations equal average surface chemical species concentrations and (2) the surface is composed only of terraces and steps. The first assumption states that a value near unity for the proportionality factor relating step site speciation to overall surface speciation appears correct because stability constants depend most strongly on specific chemical bond formation and only secondarily on longer range effects. For this reason, stability constants of aqueous chemical species are often similar to surface complexation binding constraints (Van Cappellen et al., 1993). In this regard, the thermodynamic chemical differences in bond strength are expected to be minor between terrace and step positions, so the proportionality factor should be near unity. The large kinetic differences occur due to the fewer lattice linkages at step positions, as compared with terrace positions. The second physical consideration is that charge-potential relationships at the surface provide electrostatic controls that disfavor the accumulation or depletion of charge at steps relative to terraces. The two implicated surface species affect charge directly as in the case of $>MnOH_2^+$ or indirectly as in the case of $>CO_3H$, in as much as $>CO_3H$ formation annihilates a charged $>CO_3^-$ group. Figure 10 provides a pictorial representation of surface speciation on terraces and steps, according to the SCM modeling results given in Figure 6. When the obtuse and acute step lengths per unit area are equal, as expected from the symmetry of rhodochrosite, we have $\chi_{co} = \chi_{ca} = \chi_{mo} = \chi_{ma}$, which we call $\chi_{1/2}$ hereafter. The total surface coverage by active sites is then $2\chi_{1/2}[>CO_3H] + 2\chi_{1/2}[>MnOH_2^+]$. Because the proportionality factors are near unity, it follows that the quantity $2\chi_{1/2}$ is the fraction of the surface covered by steps.

The second assumption is that the surface is entirely composed of terrace and step sites. The average surface slope is then given as follows:

$$\Delta h/\Delta l = (1 - 2\chi_{1/2})(\Delta h/\Delta l)_{terrace} + 2\chi_{1/2}(\Delta h/\Delta l)_{step} \quad (14)$$

Because the rhombohedral unit cell is isotropic, step sites have unity slope (i.e., $(\Delta h/\Delta l)_{step} = 1$). By definition, terrace sites have null slope (i.e., $(\Delta h/\Delta l)_{terrace} = 0$). Thus, $\Delta h/\Delta l = 2\chi_{1/2}$. Employing $\Delta h/\Delta l = 0.03 \pm 0.01$, we obtain $\chi_{1/2} = 0.015 \pm 0.005$. We compare the value of $2\chi_{1/2}$ with literature reports, as follows. Along a line on the surface, on average 1 in 30 atomic positions is a step site. The atomic spacing between the carbonate and the manganese groups is 3 Å on the $(10\bar{1}4)$ face of rhodochrosite. It follows that the average spacing between atomic steps is 90 Å, which corresponds to 110 steps μm^{-1}. Jordan and Ramensee (1998) report a step density measurement on the $(10\bar{1}4)$ face of calcite of 120 μm^{-1} in regions dominated by etch pits. Liang and Baer (1997) estimate the step density of $(10\bar{1}4)$ face of calcite as 20 μm^{-1}. Our value for rhodochrosite falls between these estimates for calcite.

By using $\chi_{1/2} = 0.015$, we obtain rate coefficients of $k_{co} = 2.7\ s^{-1}$, $k_{ca} = 2.1 \times 10^{-1}\ s^{-1}$, $k_{mo} = 4.1 \times 10^{-2}\ s^{-1}$, and $k_{ma} = 3.7 \times 10^{-2}\ s^{-1}$. The rate law is

$$R_{SSCM} = \chi_{1/2}(k_{co} + k_{ca})[>CO_3H] + \chi_{1/2}(k_{mo} + k_{ma})[>MnOH_2^+] \quad (15)$$

which follows from Eqn. 11. An important implication of Eqn. 15, under chemical conditions when it and its derivation hold, is that $\chi_{1/2}$ is a characteristic value of the surface: after the initial stages of dissolution the $(10\bar{1}4)$ face converges on a characteristic value of $\chi_{1/2}$, regardless of pH and initial surface morphology, at least over our range of experimental conditions.

4.3.3. Physical Meaning of k_{co}, k_{ca}, k_{mo}, and k_{ma}

It is important to consider the physical meaning of the SSCM rate coefficients k_{co}, k_{ca}, k_{mo}, and k_{ma}, which hereafter are collectively denoted as k_i. Kink-kink annihilation (KKA), which is a molecular level GM model, successfully explains the dissolution of calcium and magnesium carbonates (Liang et al., 1996a,1996b; Jordan et al., 2001). In this model, double-kink sites initiate on step edges and single-kinks then propagate bidirectionally along the step until annihilation with another kink or step termination. The net result of these two processes, which are depicted in Figure 11, is step retreat. The SSCM rate

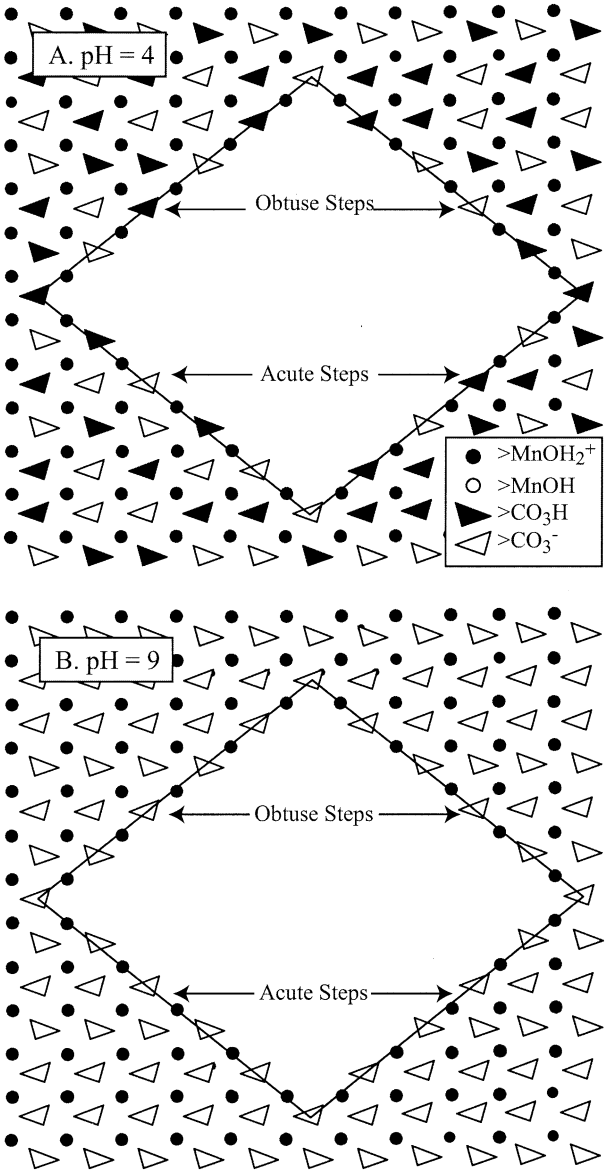

Fig. 10. Speciation of the $(10\bar{1}4)$ surface of rhodochrosite with a etch pit at (A) pH = 4 and (B) pH = 9. Dark markers indicate the dissolution active, protonated species (i.e., $>CO_3H$ and $>MnOH_2^+$). The position of atoms assumes no surface reconstruction.

coefficients k_i thus reflect the net behavior of double-kink initiation and single-kink propagation.

The KKA model is formulated quantitatively, as follows (Liang et al., 1996a,1996b):

$$\text{obtuse} \quad \nu_o = b[i_o(r_{oo} + r_{oa})]^{1/2} \tag{16a}$$

$$\text{acute} \quad \nu_a = b[i_a(r_{aa} + r_{oa})]^{1/2} \tag{16b}$$

where b is the lattice parameter ($b = 6.1 \times 10^{-10}$ m for $MnCO_3$), i_o and i_a are the respective double-kink initiation rates (s^{-1}) on obtuse and acute steps, and r_{oo}, r_{oa}, and r_{aa} are the single-kink propagation rates (s^{-1}) along the crystallographically inequivalent step directions, including obtuse-obtuse (*oo*), obtuse-acute (*oa*), and acute-acute (*aa*) (cf. Fig. 11; Liang et al., 1996a,1996b; Jordan et al., 2001). Representative values are $i_o = 0.301\ s^{-1}$, $i_a = 0.129\ s^{-1}$, $r_{oo} = 330.6\ s^{-1}$, $r_{oa} = 141.2\ s^{-1}$, and $r_{aa} = 60.3\ s^{-1}$ for calcite at pH = 9 (Liang et al., 1996a; McCoy and LaFemina, 1997). Parameter values for rhodochrosite dissolution are unavailable in literature.

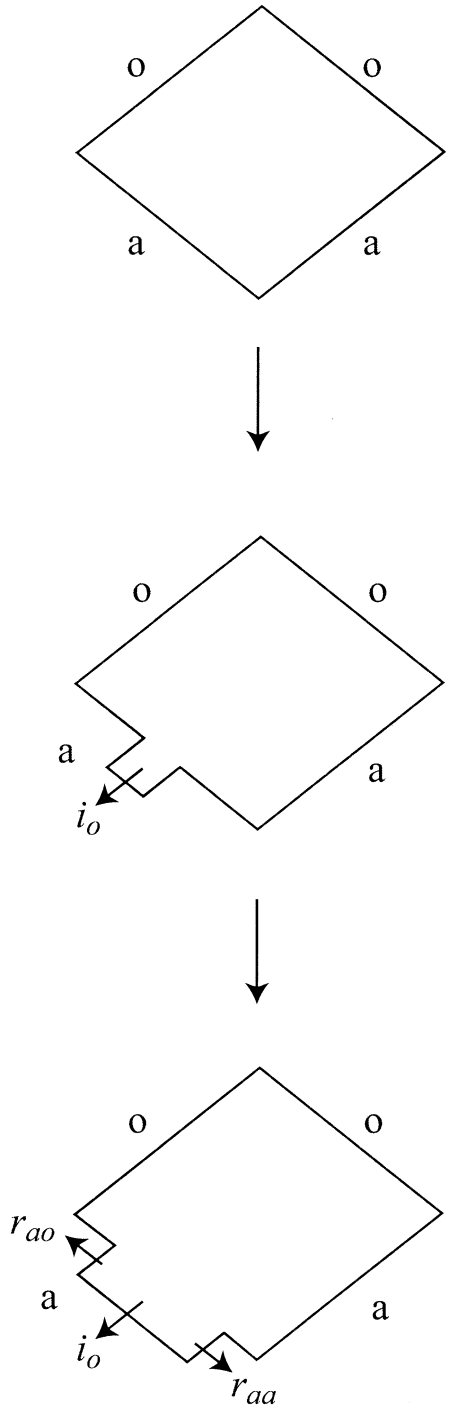

Fig. 11. Pictorial representation of double-kink initiation on a step followed by single-kink propagation.

As a limitation to the wider applicability of the current analysis to other minerals and solution conditions, the derivation of Eqn. 16 (Liang et al., 1996a,1996b) holds only for

straight steps (e.g., on ideal rhombohedral pits), which can occur only when r_{oo} and r_{oa} are similar. When for example $r_{oo} \gg r_{oa}$ as for magnesite at pH < 4.2, enrichment or depletion of kink sites causes observable changes in the obtuse step orientations away from $\langle \bar{4}41 \rangle$ and $\langle 48\bar{1} \rangle$ (Jordan et al., 2001). Pit curvature also results from deviation from the ideal KKA model. Under carbonate rich conditions, kink sites can accumulate as the r_{oo} velocity is depressed (Lea et al., 2001). Despite the limitations, the KKA model has been successfully utilized to model the expansion of rhombohedral pits (McCoy and LaFemina, 1997).

Employing the KKA model, substitution of Eqn. 16 into Eqn. 13 in the acidic regime yields:

$$\text{obtuse} \quad i_o(r_{oo} + r_{oa}) = \Phi_{co}[{>}CO_3H]^2,\ \Phi_{co} \equiv \left(\frac{k_{co}V_M}{2b}\right)^2 \tag{17a}$$

$$\text{acute} \quad i_a(r_{aa} + r_{oa}) = \Phi_{ca}[{>}CO_3H]^2,\ \Phi_{ca} \equiv \left(\frac{k_{ca}V_M}{2b}\right)^2 \tag{17b}$$

assuming $\Delta h/\Delta l = 2\chi_{1/2}$ (cf. Eqn. 14). On evaluation, $\Phi_{co} = 4.9 \times 10^9\ \mathrm{m^4\ mol^{-2}\ s^{-2}}$ and $\Phi_{ca} = 3.0 \times 10^7\ \mathrm{m^4\ mol^{-2}\ s^{-2}}$. Eqn. 17 shows that the rate coefficients k_i, which are constant so long as Eqn. 15 holds, are proportionality factors relating rates of double-kink initiation and single-kink propagation to surface chemical speciation. The effect of pH on the molecular GM parameters, including, i_o, i_a, r_{oo}, r_{oa}, and r_{aa}, is quantified by the effect on [$>CO_3H$].

Analogous results are derived in the alkaline regime for $>MnOH_2^+$, as follows:

$$\text{obtuse} \quad i_o(r_{oo} + r_{oa}) = \Phi_{mo}[{>}MnOH_2^+]^2,\ \Phi_{mo} \equiv \left(\frac{k_{mo}V_M}{2b}\right)^2 \tag{18a}$$

$$\text{acute} \quad i_a(r_{aa} + r_{oa}) = \Phi_{ma}[{>}MnOH_2^+]^2,\ \Phi_{ma} \equiv \left(\frac{k_{ma}V_M}{2b}\right)^2 \tag{18b}$$

On evaluation, $\Phi_{mo} = 1.1 \times 10^6\ \mathrm{m^4\ mol^{-2}\ s^{-2}}$ and $\Phi_{ma} = 9.1 \times 10^5\ \mathrm{m^4\ mol^{-2}\ s^{-2}}$. The conceptual implication, when Eqns. 17 and 18 are considered together, is that there is a change in mechanism for double-kink initiation and/or single-kink propagation with a change in pH due to the change from a $>CO_3H$ to a $>MnOH_2^+$-dominated regime.

Two limiting cases can be considered for the effect of [$>CO_3H$] on the rates of double-kink initiation and single-kink propagation in the acidic regime. For the first limiting case, the double-kink formation rate is taken as independent of [$>CO_3H$] and thus also of pH by implication. We then obtain

$$\text{obtuse} \quad r_{oo} + r_{oa} = \Phi'_{co}[{>}CO_3H]^2,\ \Phi'_{co} \equiv \frac{\Phi_{co}}{i_o} \tag{19a}$$

$$\text{acute} \quad r_{aa} + r_{oa} = \Phi'_{ca}[{>}CO_3H]^2,\ \Phi'_{ca} \equiv \frac{\Phi_{ca}}{i_a} \tag{19b}$$

For the second limiting case, the rate of single-kink propagation is supposed as independent of [$>CO_3H$] and again also of pH by implication. We obtain

$$\text{obtuse} \quad i_o = \Phi''_{co}[{>}CO_3H]^2,\ \Phi''_{co} \equiv \frac{\Phi_{co}}{(r_{oo} + r_{oa})} \tag{20a}$$

$$\text{acute} \quad i_a = \Phi''_{ca}[{>}CO_3H]^2,\ \Phi''_{ca} \equiv \frac{\Phi_{ca}}{(r_{aa} + r_{oa})} \tag{20b}$$

The two limiting cases indicate single-kink propagation in the first case and double-kink initiation in the second case are bimolecular in [$>CO_3H$]. Of these two possibilities, it is perhaps more intuitively satisfying to suggest that initiation is bimolecular and propagation is zero order. In this model, two protons would proximally locate on the surface (i.e., second-order in [$>CO_3H$]) to hydrolyze a surface group and thus initiate a double kink site. In reality, neither limiting case is likely completely accurate, and single-kink propagation and double-kink initiation both reasonably depend on [$>CO_3H$] and thus also pH. For example, there is some experimental evidence for $MgCO_3$ to suggest that i varies with pH (Jordan et al., 2001). We suggest, however, that in regard to Eqn. 17 when $i_o = f([{>}CO_3H])$ and $r_{oo} + r_{oa} = g([{>}CO_3H])$, we have O($f$) closer to 2 and O($g$) closer to 0, with O($f$) + O($g$) = 2.

In contrast to our understanding of k_{co}, k_{ca}, k_{mo}, and k_{ma} as a net process within the KKA model, within the SCM model the physical meaning of k is often attributed in literature as an intrinsic first-order rate constant for the rate limiting step in dissolution, which is described as metal ion detachment from the surface (Stumm and Wieland, 1990). Some support for this interpretation of k is offered by the successful correlation between k for different minerals (including carbonates) and water exchange rates of the corresponding aqueous complexes (Casey, 1991; Westrich et al., 1993; Pokrovsky and Schott, 2002). The conceptual implication is that metal ions detach from the surface as independent processes, free from cooperative effects of other nearby surface processes, just as hydrated ions exchange waters independently of proximate like-ions. This conceptual parallel may hold for more covalent minerals such as the silicates and transition metal (hydr)oxides, including iron and manganese (hydr)oxides. In contrast, ionic minerals such as the carbonates dissolve by cooperative mechanisms, as embodied in the KKA model. Because carbonate dissolution is a complex sequence of processes occurring at specific geometric sites on the surface, it could appear highly fortuitous that the correlation between dissolution rates and water exchange rates holds at all. The explanation is found in the present study through Eqn. 8, which shows that the complex KKA dissolution processes are described by a net first-order rate coefficient k and that the rate coefficient should be understood as through $\chi_{1/2}$, k_{co}, k_{ca}, k_{mo}, and k_{ma} in Eqn. 15 and those k_i coefficients in turn through i_o, i_a, r_{oo}, r_{oa}, and r_{aa} in Eqns. 17 and 18. Under this revised conceptual framework, the parameters i and r are rationalized to correlate with water exchange rates because the individual stepwise hydration reactions in double-kink initiation and single-kink propagation are energetically similar, including their kinetic activation barriers, to water exchange in aqueous metal ion complexes. The SCM dissolution model succeeds because the rates of the fundamental processes such as double-kink initiation and or single-kink propagation depend on surface chemical speciation, such as $>CO_3H$ and $>MnOH_2^+$.

5. IMPLICATIONS

In the current contribution, microscopic and macroscopic observations of rhodochrosite have been integrated to formulate a SSCM model relating the dissolution rate to the surface speciation at steps. We propose that the SSCM model may have general applicability for dissolution far from equilibrium of flat mineral surfaces of ionic crystals, at least those that dissolve by step retreat.

These insights on the dissolution process are important because rhodochrosite is a widespread and geochemically significant mineral. Rhodochrosite occurs in arid calcareous soils (Lebron and Suarez, 1999) and marine, estuarine, and lacustrine sediments (McBride and Kung, 1991; Sternbeck, 1997; Sternbeck and Sohlenius, 1997). Thermodynamic calculations indicate that rhodchrosite limits manganese solubility in anoxic waters with high alkalinity (Morgan, 1967; Jensen et al., 2002), and field measurements have found that manganese carbonate can regulate the aqueous manganese concentration in calcareous aquifers (Amirbahman et al., 1998) and in anoxic marine pore waters (Li et al., 1969; Cavert and Price, 1972; Middelburg et al., 1987). The thermodynamic and kinetic properties of rhodochrosite affect the availability of aqueous Mn^{2+} and, through coupling to aqueous Mn^{2+}, the Mn^{III}-Mn^{IV} (hydr)oxides. Precipitation and aging of insoluble Mn^{III}-Mn^{IV} oxides leads to the coprecipitation and sequestration of trace metals (Hem, 1978; Hem et al., 1989). Manganese oxides also affect the formation and degradation of humic substances (Huang, 1991; Sunda and Kieber, 1994) and the degradation of organic pollutants (Stone and Morgan, 1984; Stone, 1987). Bioavailable manganese, which is influenced by the cycling of Mn among $MnCO_3$, Mn^{2+}(aq), and Mn^{III}-Mn^{IV} (hydr)oxides, is an extremely important trace element in natural systems. It is an essential nutrient utilized as a terminal electron acceptor for microorganisms (Maier et al., 1999), in the photosynthetic pathway of green plants (Ehrlich, 1996), and in the metalloenzymes and the biomolecules of many organisms (Fruton and Simmonds, 1959).

Acknowledgments—Samples of rhodochrosite were provided by the Harvard University Mineralogical Museum. Carl Francis lent his expertise in selecting the rhodochrosite samples. Sherry Samson and Young-Shin Jun provided discussion valuable to this work. We also thank three anonymous reviewers for their insightful contributions. O.W.D. was funded by a United States Environmental Protection Agency Science to Achieve Results (USEPA STAR) Fellowship and a Sandia National Laboratories Campus Executive Program Fellowship. We are grateful for support received from the New York Community Trust Merck Fund and the Harvard University Tozier Fund.

Associate editor: D. L. Sparks

REFERENCES

Amirbahman A., Schoenberger R., Johnson C., and Sigg L. (1998) Aqueous- and solid-phase biogeochemistry of a calcareous aquifer system downgradient from a municipal solid waste landfill (Winterthur, Switzerland). *Environ. Sci. Technol.* **32,** 1933–1940.

Booth J., Hong Q., Compton R. G., Prout K., and Payne R. M. (1997) Gypsum overgrowths passivate calcite to acid attack. *J. Coll. Inter. Sci.* **192,** 207–214.

Bosbach D. and Rammensee W. (1994) In situ investigation of growth and dissolution on the (010) surface of gypsum by scanning force microscopy. *Geochim. Cosmochim. Acta* **58,** 843–849.

Brown G. E. Jr., Henrich V. E., Casey W. H., Clark D. L., Eggleston C. M., Felmy A. R., Goodman D. W., Grätzel M., Maciel G., McCarthy M. I., Nealson K. H., Sverjensky D. A., Toney M. F., and Zachara J. M. (1999) Metal oxide surfaces and their interactions with aqueous solutions and microbial organisms. *Chem. Rev.* **99,** 77–174.

Burton W. K., Cabrera N., and Frank F. C. (1951) The growth of crystals and the equilibrium structure of their surfaces. *Phil. Trans. R. Soc. Lond. Ser. A.* **243**(A.866), 299–358.

Busenberg E. and Plummer L. N. (1986) *A Comparative Study of the Dissolution and Crystal Growth Kinetics of Calcite and Aragonite.* Bulletin 1578. U.S. Geological Survey.

Casey W. H. (1991) On the relative dissolution rates of some oxide and orthosilicate minerals. *J. Coll. Int. Sci.* **146,** 586–589.

Cavert S. and Price N. (1972) Diffusion and reaction profiles of dissolved manganese in the pore waters of marine sediments. *Earth. Planet. Sci. Lett.* **16,** 245–9.

Charlet L., Wersin P., and Stumm W. (1990) Surface charge of $MnCO_3$ and $FeCO_3$. *Geochim. Cosmochim. Acta* **54,** 2329–2336.

Chou L., Garrels R. M., and Wollast R. (1989) Comparative study of the kinetics and mechanisms of dissolution of carbonate minerals. *Chem. Geol.* **78,** 269–282.

Compton R. G. and Pritchard K. L. (1990) The dissolution of calcite at pH > 7: Kinetics and mechanisms. *Phil. Trans. R. Soc. Lond. Ser. A.* **330,** 47–70.

Dresel P. E. (1989) The dissolution kinetics of siderite and its effect on acid mine drainage. Ph.D. thesis. Pennsylvania State University.

Duckworth O. W. and Martin S. T. (2001) Surface complexation and dissolution of hematite by C_1-C_6 dicarboxylic acids at pH = 5.0. *Geochim. Cosmochim. Acta* **23,** 4289–4302.

Dzombak D. A. and Morel F. M. M. (1990) *Surface Complexation Modeling.* Wiley, New York.

Eggleston C., Higgins S., and Maurice P. (1998) Scanning probe microscopy of environmental interfaces. *Environ. Sci. Technol.* **32,** 456A–459A.

Ehrlich H. L. (1996) *Geomicrobiology.* Marcel Dekker, New York.

Fenter P., Geissbuhler P., DiMasi E., Srajer G., Sorensen L. B., and Sturchio N. C. (2000) Surface speciation of calcite observed in situ by high-resolution X-ray reflectivity. *Geochim. Cosmochim. Acta* **64,** 1221–1228.

Fruton J. S. and Simmonds S. (1959) *General Biochemistry.* Wiley, New York.

Goldberg S. (1992) Use of surface complexation models in soil chemical systems. *Adv. Agron.* **47,** 233–329.

Gratz A. J., Manne S., and Hansma P. K. (1991) Atomic force microscopy of atomic-scale ledges and etch pits formed during dissolution of quartz. *Science* **251,** 1343–1346.

Hem J. (1978) Redox processes at surfaces of manganese oxide and their effects on aqueous metal ions. *Chem. Geol.* **21,** 199–218.

Hem J., Lind C., and Roberson C. (1989) Coprecipitation and redox reactions of manganese oxides with copper and nickel. *Geochim. Cosmochim. Acta* **53,** 2811–2822.

Hillner P. E., Gratz A. J., Manne S., and Hansma P. K. (1992) Atomic-scale imaging of calcite growth and dissolution in real time. *Geology* **20,** 359–362.

Hirth J. P. and Lothe J. (1982) *Theory of Dislocations.* McGraw Hill, New York.

Hong Q., Suarez M. F., Coles B. A., and Compton R. G. (1997) Mechanisms of solid/liquid interfacial reactions. The maleic acid driven dissolution of calcite: An atomic force microscope study under defined hydrodynamic conditions. *J. Phys. Chem. B.* **101,** 5557–5564.

Huang P. (1991) Kinetics of redox reactions on manganese oxides and its impact on environmental quality. In *Rates of Soil Chemical Processes* (eds. D. Sparks and D. Suarez), pp. 191–230. Soil Science Society of America, Madison, WI.

Jensen D., Boddum J., Tjell J., and Christensen T. (2002) The solubility of rhodochrosite ($MnCO_3$) and siderite in anaerobic aquatic environments. *Appl. Geochem.* **17,** 503–511.

Jordan G. and Rammensee W. (1996) Dissolution rates and activation energy for dissolution of brucite (001): a new method based on the microtopography of crystal surfaces. *Geochim. Cosmochim. Acta* **60,** 5055–5062.

Jordan G. and Rammensee W. (1998) Dissolution rates of calcite (10-14) obtained by scanning force microscopy: Microtopography-based dissolution kinetics on surfaces with anisotropic step velocities. *Geochim. Cosmochim. Acta* **62,** 941–947.

Jordan G. H., Higgins S. R., Eggleston C. M., Knauss K. G., and Schmahl W. W. (2001) Dissolution kinetics of magnesite in acidic aqueous solution, a hydrothermal atomic force microscopy (HAFM) study: step orientation and kink dynamics. *Geochim. Cosmochim. Acta* **65,** 4257–4266.

Lasaga A. C. (1998) *Kinetic Theory in the Earth Sciences.* Princeton University Press, Princeton, NJ.

Lea A. S., Amonette J. E., Baer D. R., Liang Y., and Colton N. G. (2001) Microscopic effects of carbonate, manganese, and strontium ions on calcite dissolution. *Geochim. Cosmochim. Acta* **65,** 369–379.

Lebron I. and Suarez D. L. (1999) Mechanisms and precipitation rate of rhodochrosite at 25°C as affected by P_{CO2} and organic ligands. *Soil Sci. Am. J.* **63,** 561–568.

Li Y., Bischoff J., and Mathieu G. (1969) The migration of manganese in the Arctic basin sediment. *Earth. Planet. Sci. Lett.* **7,** 265–270.

Liang Y., Baer D. R., McCoy J. M., Amonette J. E., and LaFemina J. P. (1996a) Dissolution kinetics at the calcite–water interface. *Geochim. Cosmochim. Acta* **60,** 4883–4887.

Liang Y., Baer D. R., McCoy J. M., and LaFemina J. P. (1996b) Interplay between step velocity and morphology during the dissolution of $CaCO_3$ surface. *J. Vac. Sci. Technol.* **14,** 1368–1375.

Liang Y. and Baer D. R. (1997) Anisotropic dissolution at the $CaCO_3$ $(10\bar{1}4)$–water interface. *Surf. Sci.* **373,** 275–287.

MacInnis I. N. and Brantley S. L. (1992) The role of dislocations and surface morphology in calcite dissolution. *Geochim. Cosmochim. Acta* **56,** 1113–1126.

Maier R. M., Pepper I. L., and Gerba C. P. (1999) *Environmental Microbiology.* Academic Press, New York.

McBride M. B. and Kung K. (1991) Adsorption of phenol and substituted phenols by iron oxides. *Environ. Toxicol. Chem.* **10,** 441–448.

McCoy J. M. and LaFemina J. P. (1997) Kinetic Monte Carlo investigation of pit formation at the $CaCO_3$ $(10\bar{1}4)$ surface-water interface. *Surf. Sci.* **373,** 288–299.

Middelburg J., De Lange G., and Van Der Weijden C. (1987) Manganese solubility control in marine porewaters. *Geochim. Cosmochim. Acta* **51,** 759–763.

Morgan J. (1967) Chemical equilibria and kinetic properties of manganese in natural water. In *Principles and Applications of Water Chemistry* (eds. S. Faust and J. Hunter), pp. 561–623. Wiley, New York.

Morse J. W. (1983) The kinetics of calcium carbonate dissolution and precipitation. In *Carbonates: Mineralogy and Chemistry*, Vol. 11 (ed. R. J. Reeder), pp. 227–264. Mineralogical Society of America, New York.

Orme C., Noy A., Wierzbicki A., McBride M., Grantham M., Teng H., Dove P., and DeYoreo J. (2001) Formation of chiral morphologies through selective binding of amino acids to calcite surface steps. *Nature* **411,** 775–779.

Plummer L. N., Packhurst D. L., and Wigley T. L. M. (1979) Critical review of the kinetics of calcite dissolution and precipitation. In *Chemical Modeling: Speciation, Sorption, Solubility, and Kinetics in Aqueous Systems* (ed. E. Jenne), pp. 537–573. American Chemical Society, Washington, DC.

Pokrovsky O. S. and Schott J. (1999) Processes at the magnesium bearing carbonates/solution interface. II. Kinetics and mechanisms of magnesite dissolution. *Geochim. Cosmochim. Acta* **63,** 881–897.

Pokrovsky O. S., Schott J., and Thomas F. (1999a) Dolomite surface speciation and reactivity in aquatic systems. *Geochim. Cosmochim. Acta* **63,** 3133–3143.

Pokrovsky O. S., Schott J., and Thomas F. (1999b) Processes at the magnesium bearing carbonates/solution interface. I. A surface speciation model for magnesite. *Geochim. Cosmochim. Acta* **63,** 863–880.

Pokrovsky O. S. and Schott J. (2002) Surface chemistry and dissolution kinetics of divalent metal carbonates. *Environ. Sci. Technol.* **36,** 426–432.

Rickard D. and Sjoberg S. (1983) Mixed kinetics control of calcite dissolution rate. *Am. J. Sci.* **283,** 815–830.

Samson S. D., Stillings L. L., and Eggleston C. M. (2000) The Depletion and Regeneration of. Dissolution-active sites at the mineral–water interface: I. Fe, Al, and In Sesquioxides. *Geochim. Cosmochim. Acta* **64,** 3671–3684.

Schecher W. (2001) Thermochemical data used in MINEQL+ version 4.5 with comparisons to versions 4.07 and earlier. Environmental Research Software, Hallowell, ME.

Schott J., Brantley S. L., Crerar D., Guy C., Borcsik M., and Williame C. (1989) Dissolution kinetics of strained calcite. *Geochim. Cosmochim. Acta* **53,** 373–382.

Shiraki R., Rock P. A., and Casey W. H. (2000) Dissolution kinetics of calcite in 0.1 M NaCl solution at room temperature: an atomic force microscope study. *Aquat. Geochem.* **6,** 87–108.

Sternbeck J. (1997) Kinetics of rhodochrosite crystal growth at 25°C: the role of surface speciation. *Geochim. Cosmochim. Acta* **61,** 785–793.

Sternbeck J. and Sohlenius G.(1997) Authingeic sulfide and carbonate mineral formation in Holocene sediments of the Baltic Sea. *Chem. Geol.* **135,** 55–73.

Stipp S. L. S., Eggleston C. M., and Nielsen B. S. (1994) Calcite surface structure observed at microtopographic and molecular scales with atomic force microscopy (AFM). *Geochim. Cosmochim. Acta* **58,** 3023–3033.

Stone A. T. (1987) Reductive dissolution of Mn(III/IV) oxides by substituted phenols. *Environ. Sci. Technol.* **21,** 979–988.

Stone A. and Morgan J. (1984) Reduction and dissolution of manganese(III) and manganese(IV) oxides by organics: 1. Reaction with hydoquinone. *Environ. Sci. Technol.* **18,** 450–456.

Stumm W. (1992) *Chemistry of the Solid–Water Interface*. Wiley, New York.

Stumm W., Furrer G., Wieland E., and Zinder B. (1985) The effect of complex-forming ligands on the dissolution of oxides and aluminosilicates. In *The Chemistry of Weathering* (ed. J. I. Drever), pp. 55–74. D. Reidel Publishing, Hingham, MA.

Stumm W. and Furrer G. (1987) The dissolution of oxides and aluminium silicates; examples of surface-coordination-controlled kinetics. In *Aquatic Surface Chemistry* (ed. W. Stumm), pp. 197–217. Wiley, New York.

Stumm W. and Wieland E. (1990) Dissolution of oxide and silicate minerals: rates depend on surface speciation. In *Aquatic Chemical Kinetics* (ed. W. Stumm), pp. 367–400. Wiley, New York.

Stumm W. and Morgan J. J. (1996) *Aquatic Chemistry*. Wiley, New York.

Sunda W. and Kieber D. (1994) Oxidation of humic substances by manganese oxides yields low-molecular weight organic substrates. *Nature* **367,** 62–64.

Teng H. H. and Dove P. M. (1997) Surface site-specific interactions of aspartate with calcite during dissolution: implications for biomineralization. *Am. Mineral* **82,** 878–887.

Teng H. H., Dove P. M., Orme C. A., and De Yoreo J. J. (1998) Thermodynamics of calcite growth: baseline for understanding biomineral formation. *Science* **282,** 724–727.

Teng H. H., Dove P. M., and De Yoreo J. J. (2000) Kinetics of calcite growth: Surface processes and relationships to macroscopic rate laws. *Geochim. Cosmochim. Acta* **64**, 2255–2266.

Van Cappellen P., Charlet L., Stumm W., and Wersin P. (1993) A surface complexation model of the carbonate mineral-aqueous solution interface. *Geochim. Cosmochim. Acta* **57,** 3505–3518.

Westrich H. R., Cygan R. T., Casey W. H., Zemitis C., and Arnold G. W. (1993) The dissolution kinetics of mixed-cation orthosilicate minerals. *Am. J. Sci.* **293,** 869–893.

APPENDIX

List of Symbols

A, surface area (m^2)
b, spacing between manganese and carbonate centers in the lattice (m)
i_x, rate of double-kink initiation on a step (s^{-1})
GM, geometric model
$\Delta h/\Delta l$, characteristic slope of the surface

k_{xy}, dissolution rate coefficient of a chemical surface species at a step (s^{-1})
$k_x^{'}$, dissolution rate coefficient of a chemical surface species (s^{-1})
K_{sp}, solubility product (M^2)
KKA, kink–kink annihilation
MM, mechanistic model
n_c, reaction order for the $>CO_3H$ dissolution pathway
n_m, reaction order for the $>MnOH_2^+$ dissolution pathway
N, number of AFM images collected in a dissolution experiment
q, flow rate ($L\ s^{-1}$)
Q, reaction quotient (m^2)
r_{xy}, rate of single-kink propagation along a step in the x-y direction (s^{-1})
R, dissolution rate ($mol\ m^{-2}\ s^{-1}$)
R_{mic}, dissolution rate as calculated from AFM images ($mol\ m^{-2}\ s^{-1}$)
R_{mac}, dissolution rate as calculated from aqueous manganese flux ($mol\ m^{-2}\ s^{-1}$)
SCM, surface complexation model
SSCM, step-site surface complexation model
V_M, molar volume ($m^3\ mol^{-1}$)
Δx_i, change in a lateral etch pit dimension (m) from AFM image i to image $i + 1$
κ, capacitance of the rhodochrosite–water interface ($F\ m^{-2}$)
ν_x, step retreat rate ($m\ s^{-1}$)
ν_{avg}, average step retreat rate ($m\ s^{-1}$)
σ, surface charge ($C\ m^{-2}$)
τ, acquisition time for an AFM image (s)
Φ_{xy}, rate coefficient of a surface chemical species on a step ($m^4\ mol^{-2}\ s^{-2}$)
χ_{xy}, fraction of surface sites associated with steps
χ, fraction of surface chemical groups associated with active sites ($2\chi_{1/2}$)
$\chi_{1/2} = \chi_{co}, \chi_{ca}, \chi_{mo}, \chi_{ma}$
[>X], concentration of surface chemical group X ($mol\ m^{-2}$)

Subscripts *x* and *y*

a, acute step
c, $>CO_3H$ surface chemical group
m, $>MnOH_2^+$ surface chemical group
o, obtuse step